

Chromophore Orientations upon Irradiation in Gratings Inscribed on Azo-Dye Polymer Films: A Combined AFM and Confocal Raman Microscopic Study

F. Lagugné Labarthe, J. L. Bruneel, T. Buffeteau, and C. Sourisseau*

LPCM, UMR 5803, CNRS, Université de Bordeaux 1, 351 cours de la Libération,
33405 Talence Cedex, France

Received: July 23, 2003; In Final Form: February 4, 2004

Diffraction gratings of weak efficiency ($\approx 2\text{--}3\%$) were inscribed on thin films of the azobenzene p(DR1M) homopolymer using orthogonal linear ($+45^\circ, +135^\circ$) polarizations of two coherent laser beams. After an erasure process using a single beam of circular polarization ("RCP"), the surface relief profiles measured from atomic force microscopy (AFM) were compared on a grating inscribed during a short time period (≈ 200 s) and on similar gratings tentatively erased with a "RCP" irradiation during a short (100 s) or a long (800 s) period. In addition, confocal micro-Raman polarized experiments were performed on these gratings and, using a rigorous treatment of the Raman intensity variations, the two even parity Legendre polynomials or parameter orders, $\langle P_2 \rangle$ and $\langle P_4 \rangle$, were estimated in the well, slope, and peak regions of the surface relief gratings; the corresponding forms of the most probable chromophore orientation distribution functions were determined. It is thus concluded that the variations in diffraction efficiency observed at short time are not due to any change in the amplitude of the surface relief modulation (equal to $\approx 112\text{--}110$ nm) but to a significant increase in the birefringence contributions; the chromophore distribution functions become largely anisotropic. Then, the orientational anisotropy is partly maintained during the poorly efficient erasing process, and after a longer time irradiation, the final relief amplitude is found equal to 66–70 nm. In the p(DR1M) polymer system under study, the ($+45^\circ, +135^\circ$) linear polarization configuration thus appears very suitable for single beam duplication experiments and/or for further phase mask applications.

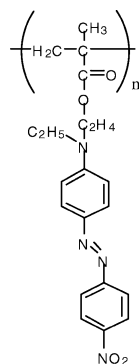
I. Introduction

The direct recording of diffraction gratings on polymer thin films functionalized with azobenzene molecules is still the subject of intense studies. Interest is mainly due to the possibility to inscribe both birefringence (phase) and surface relief (amplitude) gratings without pre- or postprocessing and to get high diffraction efficiencies, η , on the ± 1 orders (η is the intensity ratio of the ± 1 diffracted order over the zero order transmitted beam) with a good thermal stability. Following the pioneering and independent works of Rochon et al.^{1–3} and of Tripathy et al.,^{4–6} numerous studies on various polymer systems have been performed by several groups;^{7–33} it has been demonstrated that large surface modulations from a few hundreds of nanometers up to the micron scale, i.e., up to twice the initial film thickness, could be inscribed on azopolymer thin films. Generally, an argon ion laser radiation at a wavelength of about 500 nm with a moderate irradiance (a few tens of mW/cm²) was used to record the grating. Also, the formation process of a grating was found to be strongly dependent on the polarization and on the laser fluence, and it has been established that thermal effects do not play any role in the formation of the sinusoidal surface relief. When using azobenzene functionalized polymer films, instead of dye-doped polymer systems, it has also been shown that the surface gratings are very stable and permanent at below the glass transition temperature (T_g) of the polymer. Therefore, the gratings can be erased either by heating the sample above T_g or by irradiation with a single laser beam of appropriate wavelength and polarization.^{34–39} Results about single beam optical erasures of surface relief gratings have been scarcely published in the

literature, but a quite unusual polarization dependent effect has already been reported for thin films of an epoxy based side-chain azobenzene polymer (called PDO3 in ref 35). In this PDO3 example, the erasure dynamics were found to be strongly dependent on the erasing pump polarization, and the surface relief grating once formed was behaving as a "memory" of the states which created it; accordingly, some gratings were found to be very stable. Consequently, the authors have accomplished with success a reproduction or direct transfer of patterns by photoprinting through such a phase mask. Actually, phase masks can be used in a wide range of applications to create periodic intensity modulation of light, to reconfigure optical recording media, and/or to simply achieve direct photoprinting of stable microstructures.^{40–42} So, it is of great interest not only to check if similar masks can be created using other polymer systems but also to get a better understanding into the formation and erasure mechanisms of the gratings. Indeed, such an all-optical process could be a new alternative route, instead of using pattern transfer techniques more often based on lithographical methods.^{43–45} Furthermore, these high-density erasable holographic memories could provide a rapid access to stationary blocks of media in various modern communication applications.⁴⁶

In this respect, we have recently paid attention to the formation of various holographic gratings in thin films of the p(DR1M) homopolymer, with diffraction efficiencies (measured on the ± 1 orders) ranging from 0.5 to nearly 30%, and to the dynamics of their erasures upon irradiation with a vertical (s), horizontal (p) linearly, or right circularly (RCP) polarized single laser beam.³⁹ Our main goal was to find the best conditions to preserve the regularly modulated relief surfaces of the gratings

* To whom correspondence should be addressed. Fax: (33) 5 40 00 84 02. E-mail: c.sourisseau@lpcm.u-bordeaux1.fr.

SCHEME 1: Chemical Formula of the p(DR1M) Homopolymer


and to show their potential in duplication and phase mask applications.

Now, to address this problem from the point of view of the chromophore orientation properties, we have made use of the confocal micro-Raman scattering spectrometry, which is known as a very sensitive non destructive technique with a high spectral and spatial resolution. In fact, we have recently demonstrated in several micro-Raman studies^{16,19,20,47} that, from careful polarized Raman scattering measurements, one can get estimates of the two first-order parameters of even parity and determine the chromophore orientation functions in the different regions, well, slope, and peak, of the surface relief profile.

This paper is thus organized as follows: In the Experimental Section (II), the materials and the optical setups are first described. In section III, the grating diffraction results during the writing, relaxation, and erasing periods are presented in conjunction with the related AFM topographic data. Then, in the main section IV, the theoretical Raman intensity expressions and the important corrections to apply in confocal polarized micro-Raman studies are first recalled; then, the Raman intensity results are successively discussed in the three gratings under investigation; they are illustrated with nicely resolved Raman images and interpreted in terms of the molecular orientations via the calculation of both order parameter values, $\langle P_2 \rangle$ and $\langle P_4 \rangle$; then, using the Information Entropy model⁴⁸ the most probable distribution functions in the various regions of the relief profile are obtained and compared. Finally, in section V, we draw several important conclusions concerning the variations in the chromophore orientations during the grating inscription and after a short and a long time of irradiation with a "RCP" polarized single beam. We thus afford new information about the relative contributions of the birefringence and surface relief gratings and their constructive interferences; this may open new routes to preserve and duplicate large regular surface modulations on these polymer gratings and to develop promising applications.

II. Experimental Section

A. Materials. We have used the so-called p(DR1M) homopolymer containing a 100% molar fraction of the azobenzene DR1 derivative covalently bonded in side-chain position (see Scheme 1). Details about the synthesis and polymer characterization ($T_g = 129^\circ\text{C}$) can be found elsewhere.^{49,50} Thin films were prepared by spin coating a solution of p(DR1M) in chloroform on clean glass microscope slides and heating 30 min at 120°C . The thickness of the film was controlled by AFM (Thermomicroscope Research CP) in the contact mode by measuring the height of a step on a scratched sample (the tip was an Ultralever 06B with a force constant $F = 0.4\text{ N/m}$); the thickness was equal to $330 \pm 10\text{ nm}$.

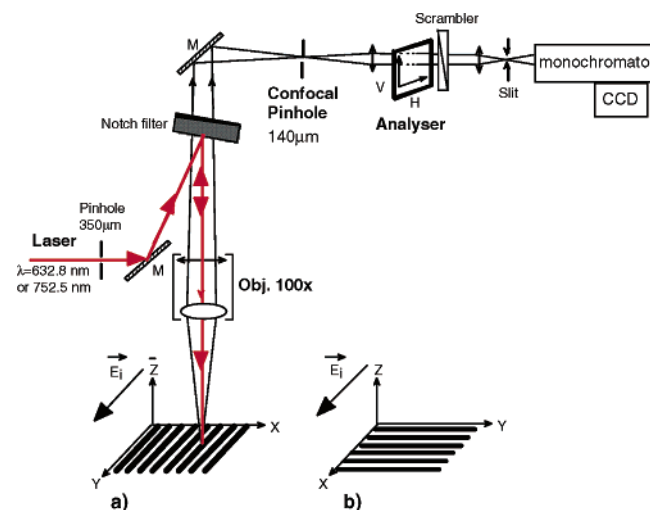
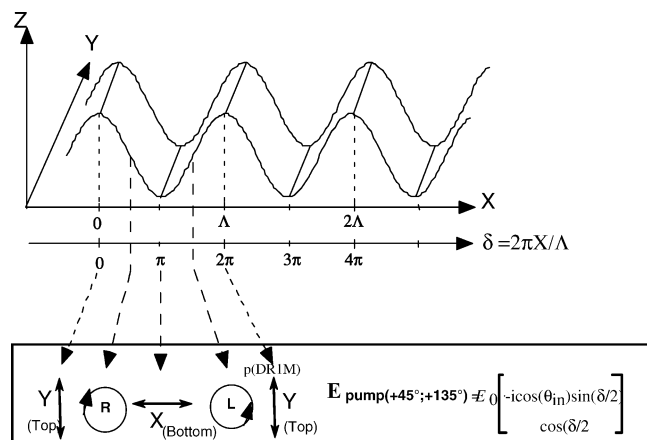


Figure 1. Experimental setup for the polarized micro-Raman measurements: (a) recording of the (YY) and (YX) spectra in the first configuration; (b) recording of the (XX) and (XY) polarized spectra in the second configuration.

B. Optical Setups. The holographic setup developed for the grating inscription has been already published.^{21,39} Briefly, it consists of a two-arm interferometer used to generate the interference pattern from an argon laser beam ($\lambda = 514.5\text{ nm}$) going through a Wollaston polarizer. The polarizations of the two emerging beams are thus adjusted using half-wave or quarter-wave retarder plates and carefully checked by using a photopolarimeter (Thorlabs); the degree of linear or circular polarization is always better than 98%. Both incident beams of equal intensity and with an irradiance of about $30\text{--}40\text{ mW/cm}^2$ (for each beam) are thus recombined onto the sample with an incidence angle (θ) equal to about $\pm 10.8^\circ$. According to Bragg's law, $2\Lambda \sin(\theta) = \lambda$, the observed grating spacing is equal to $\Lambda = 1.37\text{ }\mu\text{m}$. In all of the experiments, the time evolution of the transmitted and diffracted orders is probed by using a vertical (s) linearly polarized He-Ne laser ($\lambda_{\text{probe}} = 632.8\text{ nm}$) with a very low intensity ($I_{\text{probe}} < 0.05\text{ mW}$). The probe beam is chopped at 1 kHz and impinges the thin film normal to its surface. Two identical photodiodes are used to probe simultaneously the intensity variations of the transmitted zero- and diffracted first-order, respectively, and the signals are demodulated by using two lock-in amplifiers.

The Raman spectra were recorded in the backscattering geometry on a Labram I (Jobin-Yvon, Horiba Group, France) microspectrometer in conjunction with a confocal microscope and a $100\times$ objective lens.^{16,19,47} To avoid any thermal, photochemical or bleaching effect, we have used a minimum intensity power ($\approx 1.5\text{--}1.7\text{ mW}$) of the 752.5 nm incident line from an Ar-Kr laser. The linear polarization direction of the laser beam was fixed due to the configuration setup of the instrument, which contained a special Notch filter (at 752.5 nm) eliminating the low-frequency elastic and inelastic contributions (Figure 1). Polarization analyses were performed on the back-scattered radiation with a polarizing analyzer in the vertical (V) or horizontal (H) position and using a depolarization scrambler ($\approx \lambda/4$) in front of the entrance slit of the monochromator; the alignment and calibration of these optical elements were checked by recording the intense polarized Raman spectra of the CCl_4 liquid and also the Raman responses of a similar but isotropic thin film sample. The already inscribed $1.37\text{ }\mu\text{m}$ period grating was mounted on the XY-motorized microscope table with $\pm 0.125\text{ }\mu\text{m}$ controlled step scan displacements along the \hat{X} grating vector direction. Typically, a number of $3 \times 40 = 120$

SCHEME 2: Surface Relief Profile and Components of the Incident Electric Field upon Grating Inscription Using the (+45°, +135°) Configuration



Raman spectra were collected over three lines at different Y coordinates, each of $5.0 \mu\text{m}$ length, and the acquisition time was fixed to 5 s (or 10 s) per spectrum leading to a total run time of $120 \times 5 = 600$ s (or 1200 s). Each polarized Raman image for a selected wavenumber range (as discussed below) is thus the result of integrated intensity variations observed over the 120 recorded spectra for the area grating under inspection. Obviously, this implies a high quality of the optical setup and stability of the sample, which could be controlled at any time on a TV monitor displaying the video white light image of its surface. Finally, a high grade sensitivity air cooled CCD detector was used for detection, allowing a simultaneous spectral dispersion (from a 600 grooves/mm grating) over a wide wavenumber range (of about 2000 cm^{-1}) and the Raman shift measurements ($\pm 3 \text{ cm}^{-1}$) were calibrated using plasma lines.

III. Diffraction Results and Topographic AFM Data

For gratings inscribed using the linear (+45°, +135°) configuration, with respect to the X axis horizontal grating vector direction, the modulation of polarization is important since the resulting electric field over a half-period grating is successively linear (vertical, “s”), elliptical, circular, elliptical and linear (horizontal, “p”) and so on (see Scheme 2). Although the incident intensity is nearly constant, this setup is reported as relatively efficient for grating inscription.^{12,13,20,51} In that case, we have mainly examined the writing and erasing dynamics over short time periods for holographic gratings with a weak efficiency ($\eta \approx 2\text{--}3\%$).

As shown in Figure 2, we observe distinct regimes in the diffraction efficiency curves: first, during the initial few seconds, there is a drastic increase due to the formation of a birefringence grating which mimics the polarization pattern; then, there is a pronounced decrease due to the molecular reorientations and, probably, to destructive interferences between birefringence and surface relief contributions; finally, it appears a new significant increase due to a rapid growth of the surface modulation which becomes dominant. After a 100 s writing period, the beams are switched “off” when the diffraction efficiency is equal to $\approx 1\%$, but it increases again very rapidly, reaches a plateau value of 1.5%, and remains stable during the whole relaxation period (which is here equal to 100 s but may be longer). It is important to note that, although the diffraction power is weak in this stationary state, a large surface relief modulation equal to 110–114 nm already exists, as inferred from AFM data (Figure 3a). Then, we have intentionally used a “RCP” polarized erasing

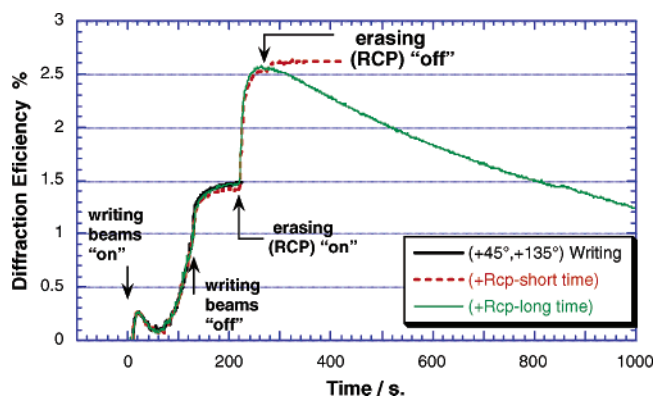


Figure 2. Time variations of the diffraction efficiency measured on the +1st order for low diffraction gratings ($\eta = 1.5\%$) inscribed under the (+45°, +135°) polarization setup and, after that irradiated using a “RCP” polarized single beam ($\eta = 2.7\%$ after a short time illumination and $\eta = 1.2\%$ after a longer time shining, respectively). Note that the diffraction increases first when the writing beams are “off” and, second, during a short period when the “RCP” single beam is “on”; an efficient erasure takes place only after a long time “RCP” irradiation.

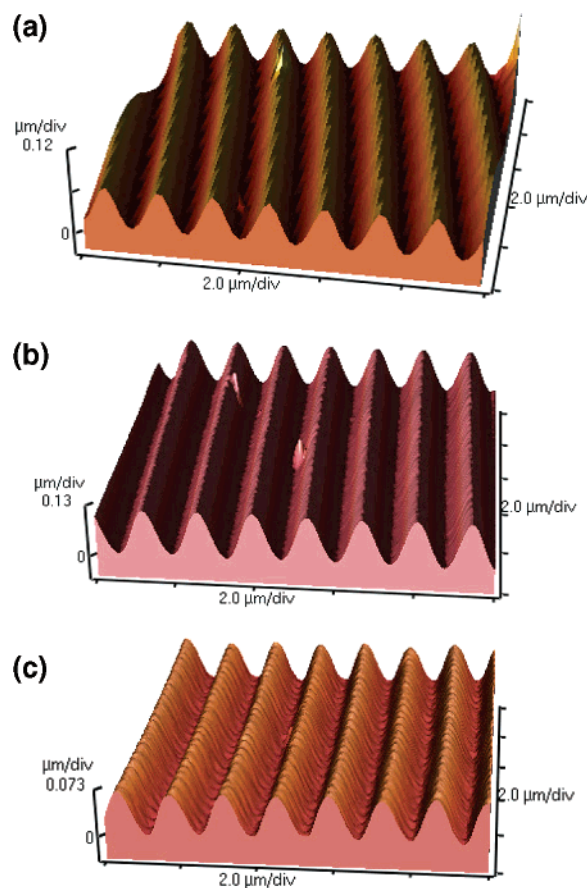


Figure 3. Topographic AFM results obtained for the first inscribed grating ($\Delta h = 114 \text{ nm}$), for the second grating after a short time “RCP” irradiation ($\Delta h = 110 \text{ nm}$), and after a longer time irradiation ($\Delta h = 66 \text{ nm}$).

single beam and compared two gratings irradiated during a 50 s short period or during a ≈ 800 s longer time period, respectively. In the first case, surprisingly, a drastic and rapid additional increase in the diffraction efficiency from 1.5% up to 2.6–2.7% is detected; this result is reproducible and has been checked in several repeated experiments. Very interestingly, the new perturbed grating is stable and permanent if the single beam is switched “off” at a short time (Figure 2). Such a behavior

seems quite peculiar, and AFM data indicate that the surface modulation has not at all changed, its amplitude being still equal to 110 nm (Figure 3b). We thus arrive to the suggestion that, during the first “RCP” irradiation following the grating inscription, the grating sample becomes more strongly anisotropic; it seems that the “RCP” beam has induced at short times new molecular orientations and created another birefringence contribution. A new phase grating, probably superimposed to the previous one, could be responsible for the last increase in the diffraction efficiency. In contrast, in the second case and after a longer time experiment of ≈ 800 s irradiation, the diffraction efficiency decreases monotonically down to 1.2% (Figure 2); the AFM data confirm that the surface modulation is markedly reduced, but the remaining relief amplitude equal to ≈ 66 nm is still significant (Figure 3c).

In conclusion, the above gratings inscribed using the linear ($+45^\circ$, $+135^\circ$) incident polarization configuration and irradiated using another circularly polarized single beam were found to be quite stable. This polarization configuration appears suitable for grating duplications, but the microscopic molecular orientation mechanisms still remain unknown. It is thus the purpose of our confocal micro-Raman study to afford new information in that direction.

IV. Raman Intensity Expressions and Confocal Micro-Raman Results

Theoretical Polarized Raman Intensity Expressions. Because of the cylindrical symmetry of azobenzene chromophores, the molecular polarizability tensor is assumed to be diagonal:

$$\bar{\alpha} = \begin{pmatrix} \alpha_1 & 0 & 0 \\ 0 & \alpha_1 & 0 \\ 0 & 0 & \alpha_3 \end{pmatrix} \quad (1)$$

Then, the molecular orientations in the grating are expected to derive primarily from the resulting electric field of the two ($+45^\circ$, $+135^\circ$) interfering laser beams (Scheme 2). According to recent theories of photoinduced anisotropy by a polarized laser beam and assuming that the angular density of “trans” chromophores is governed by an angular hole burning (AHB) process,^{52–55} and under the weak pumping limit ($J \ll 1.0$) one may write

$$n_T(\theta) \equiv \frac{N}{4\pi} (1 - J \cos^2 \theta_p) \quad (2)$$

where θ_p is the angle between the pump polarization direction and the main long axis of the chromophore. So, as recently demonstrated for thin films irradiated under the same polarization conditions and for gratings investigated from standard backscattering Raman experiments using a linearly polarized incident beam in either the parallel (Y) or in the perpendicular (X) direction (see a and b configurations in Figure 1, respectively), the intensity expressions are^{19,20,56}

$$I_{(YY)} = \frac{N}{105} \alpha_3^2 \left[(21 + 28a_1 + 56a_1^2) - J(3 + 8a_1 + 24a_1^2) - J \cos^2 \left(\frac{\delta}{2} \right) (12 + 4a_1 - 16a_1^2) \right] \quad (3)$$

$$I_{(XX)} = \frac{N}{105} \alpha_3^2 \left[(21 + 28a_1 + 56a_1^2) - J(15 + 12a_1 + 8a_1^2) + J \cos^2 \left(\frac{\delta}{2} \right) (12 + 4a_1 - 16a_1^2) \right] \quad (4)$$

where δ is the path difference between the two pumps ($\delta =$

$2\pi X/\Lambda$) and $a_1 = \alpha_1/\alpha_3$ is the ratio of the molecular polarizability coefficients, which is expected to be very weak ($\ll 1.0$) under preresonance Raman conditions. Therefore, $I_{(YY)}$ is expected to be minimum at $\delta = 0$ and maximum at $\delta = \pi$, and conversely for the $I_{(XX)}$ intensity. In contrast, under such a simple macroscopic approach, the two other crossed polarization terms $I_{(YX)}$ and $I_{(XY)}$ are not dependent on a $J \cos^2(\delta/2)$ type term, and their variations cannot be straightforwardly predicted; only an inspection of the higher order contributions in a microscopic treatment (in particular, the $I_{(YZ)}$ and $I_{(XZ)}$ terms in the general intensity equations as reported below) indicates that their intensity variations are expected to be nearly in phase in each experimental configuration. Moreover, we know that the quite similar $I_{(YX)}$ and $I_{(XY)}$ spectra are always less intense than the $I_{(YY)}$ and $I_{(XX)}$ ones. In the first set of experiments (Figure 1a), the Raman intensity ratio

$$R_1(\delta) = \frac{I_{(YX)}}{I_{(YY)}} \quad (5)$$

will thus be maximum at $\delta = 0$, 2π (at the tops of the relief) and minimum at $\delta = \pi$ (at the bottoms of the surface relief). Conversely, in the second set of experiments (Figure 1b), the ratio

$$R_2(\delta) = \frac{I_{(XY)}}{I_{(XX)}} \quad (6)$$

will be minimum at near $\delta = 0$, 2π and maximum at near $\delta = \pi$.

These results are very important, and they will allow us to properly combine and scale all of the Raman data along the \bar{X} grating vector direction, to establish the variations of the two experimental ratios. Indeed, from the R_1 and R_2 values, we shall be able to calculate the two first even parity Legendre's polynomials, i.e., the $\langle P_2 \rangle$ and $\langle P_4 \rangle$ order parameters of the chromophore orientation functions (see below). In this respect, it is also very important to underline that during the grating inscription the incident electric field is strictly circularly polarized at a quarter of period (dephasing $\delta = \pi/2$) and a three-quarter of period (dephasing $\delta = 3\pi/2$) positions (see Scheme 2), so that nearly isotropic molecular orientations should normally be retrieved at these peculiar locations.

Estimation of the $\langle P_2 \rangle$ and $\langle P_4 \rangle$ Coefficients in a Rigorous Treatment Taking into Account the Effect of the High Numerical Aperture Objective Lens. We consider now that all of the photoinduced and mass transport effects lead to anisotropic samples but with localized regions keeping an uniaxial symmetry around the resulting pump laser polarization axis contained in the film plane. In a first approximation, the angular distribution of the chromophores may be obtained by developing the function $f(\theta)$ on basis of the first even parity terms in Legendre's polynomials

$$\begin{aligned} \langle n_T \rangle &= \frac{N}{4\pi^2} \int_0^{2\pi} d\psi \int_0^{2\pi} d\varphi \int_{-1}^{+1} f(\theta) d(\cos \theta) \\ &= N \int_{-1}^{+1} \left[\frac{1}{2} \langle P_0 \rangle P_0(\cos \theta) + \frac{5}{2} \langle P_2 \rangle P_2(\cos \theta) + \frac{9}{2} \langle P_4 \rangle P_4(\cos \theta) \right] d(\cos \theta) \quad (7) \end{aligned}$$

where the coefficients $\langle P_i \rangle$ are the order parameters which for

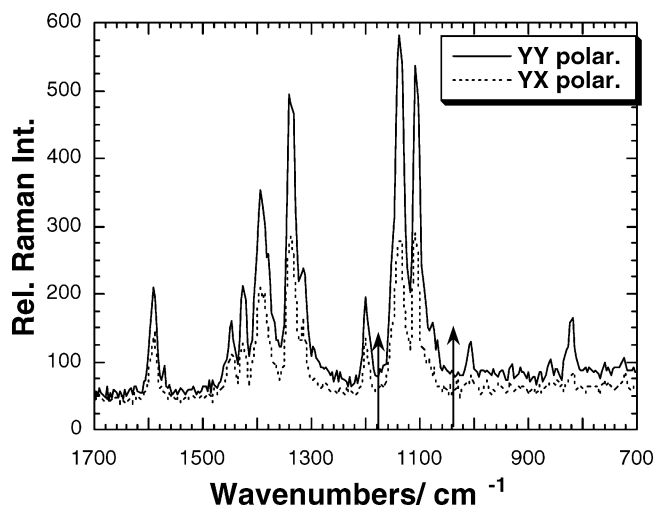


Figure 4. Typical survey (YY) and (YX) polarized Raman spectra in the 700–1700 cm^{-1} range recorded from the surface of the first grating ($\eta = 1.5\%$); the vertical arrows indicate the domain used for calculations of the integrated intensities to establish the Raman images.

full cylindrical symmetry are given by

$$\langle P_0 \rangle = 1.0, \quad \langle P_2 \rangle = \frac{1}{2} \langle 3 \cos^2 \theta - 1 \rangle,$$

$$\text{and } \langle P_4 \rangle = \frac{1}{8} \langle 35 \cos^4 \theta - 30 \cos^2 \theta + 3 \rangle \quad (8)$$

First, to extract correct values of the order parameters, in the case of ($+45^\circ, +135^\circ$) grating inscription, it is necessary to take into account changes in the direction of the incident electric field over a grating period. So, an additional rotation $R(\alpha)$ around the Z axis has to be considered over the polarizability tensor and the corresponding Raman intensities are dependent on the following average quantities

$$\langle \alpha_{ij}^2 \rangle = [R(\alpha) \{ T(\theta, \varphi, \psi) \bar{\alpha} T'(\theta, \varphi, \psi) \} R'(\alpha)]^2 \quad (9)$$

Note that a 90° rotation with respect to the grating vector direction corresponds here to δ values equal to either 0 or 2π radians (peak regions) or equivalently to X values equal to 0 or Λ (Scheme 2).

Second, we have to take into account the effect of the high numerical aperture objective. In backscattering Raman microspectrometry, it is well-known that analyses of polarization measurements must be established using the known optical properties of the wide aperture objective and the refractive index of the sample. According to Turrell et al.^{57–59} and using the $\langle \alpha_{ij}^2 \rangle$ expressions as derived above from eq 9, in the first experimental geometry (Figure 1a) we arrive to the general intensity equations

$$I_{(YX)} = [\langle \alpha_{YX}^2 \rangle A + \langle \alpha_{YZ}^2 \rangle B] (2C_0 + C_2) + [\langle \alpha_{ZX}^2 \rangle A + \langle \alpha_{ZZ}^2 \rangle B] (4C_1) + [\langle \alpha_{XX}^2 \rangle A + \langle \alpha_{XZ}^2 \rangle B] (C_2) \quad (10)$$

$$I_{(YY)} = [\langle \alpha_{YY}^2 \rangle A + \langle \alpha_{YZ}^2 \rangle B] (2C_0 + C_2) + [\langle \alpha_{ZY}^2 \rangle A + \langle \alpha_{ZZ}^2 \rangle B] (4C_1) + [\langle \alpha_{XY}^2 \rangle A + \langle \alpha_{XZ}^2 \rangle B] (C_2) \quad (11)$$

Similarly, in the second experimental configuration (Figure 1b)

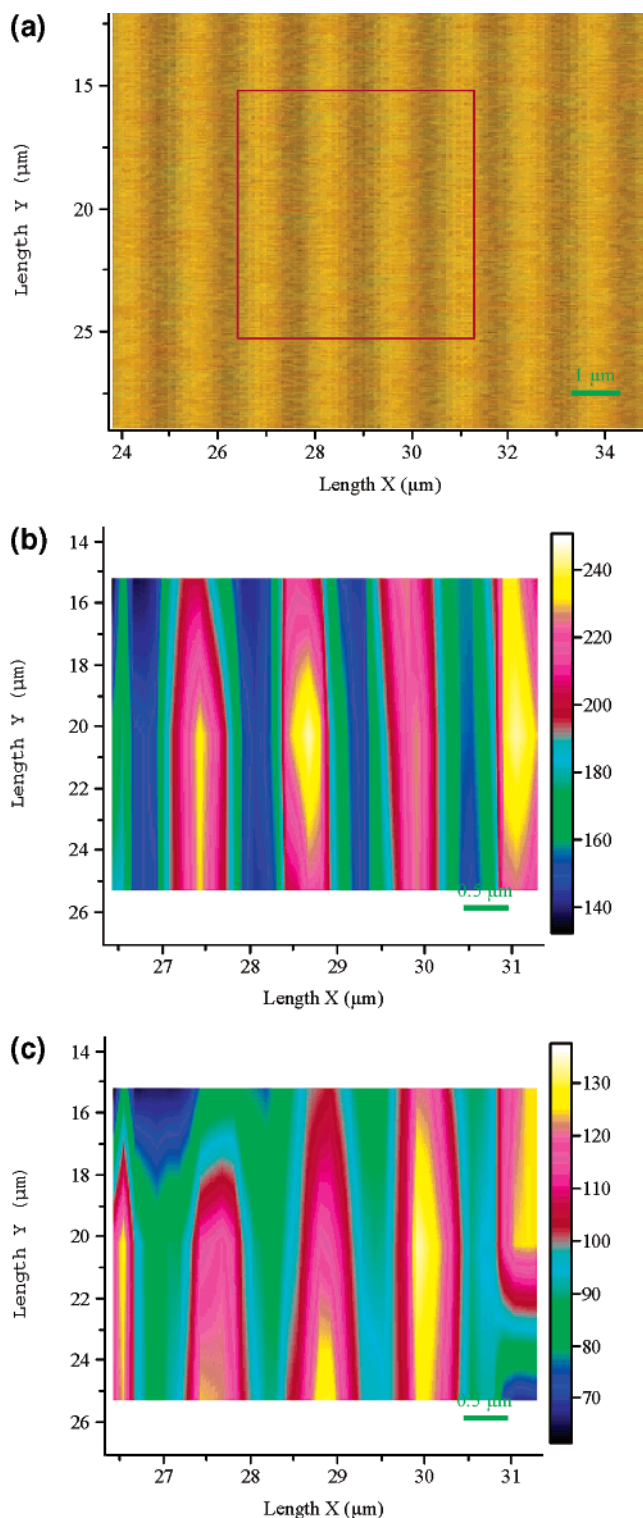


Figure 5. Video image (a) and Raman images obtained over a $5 \times 10 \mu\text{m}^2$ area of the first grating ($\eta = 1.5\%$) under (b) the (YY) and (c) the (YX) polarization conditions, using the first experimental configuration described in Figure 1a.

we obtain

$$I_{(XY)} = [\langle \alpha_{XY}^2 \rangle A + \langle \alpha_{XZ}^2 \rangle B] (2C_0 + C_2) + [\langle \alpha_{ZY}^2 \rangle A + \langle \alpha_{ZZ}^2 \rangle B] (4C_1) + [\langle \alpha_{YY}^2 \rangle A + \langle \alpha_{YZ}^2 \rangle B] (C_2) \quad (12)$$

$$I_{(XX)} = [\langle \alpha_{XX}^2 \rangle A + \langle \alpha_{XZ}^2 \rangle B] (2C_0 + C_2) + [\langle \alpha_{ZX}^2 \rangle A + \langle \alpha_{ZZ}^2 \rangle B] (4C_1) + [\langle \alpha_{YX}^2 \rangle A + \langle \alpha_{YZ}^2 \rangle B] (C_2) \quad (13)$$

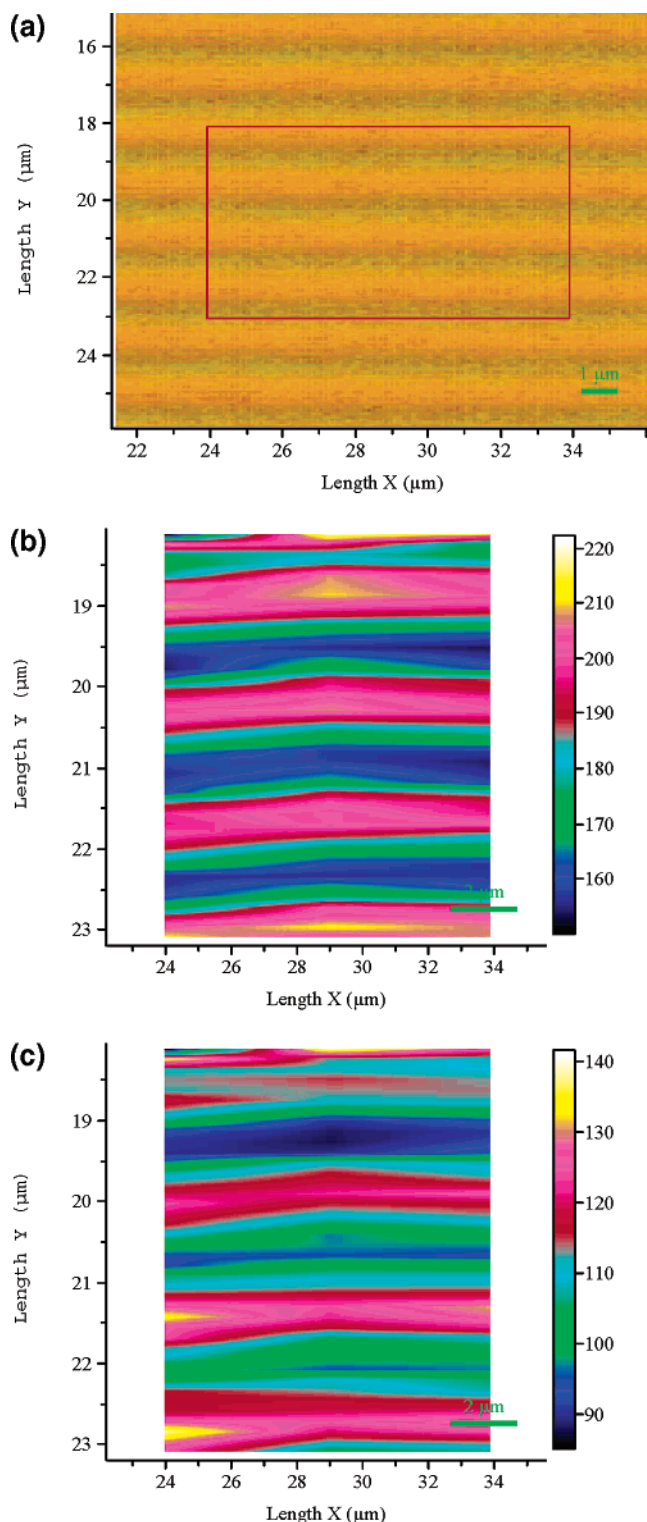


Figure 6. Video image (a) and Raman images obtained over a $5 \times 10 \mu\text{m}^2$ area of the first grating ($\eta = 1.5\%$) under (b) the (XX) and (c) the (XY) polarization conditions, using the second experimental configuration described in Figure 1b.

where the quantities A and B come from integrations of the squares of the electric vector components over the scattering cone, and the coefficients C_0 , C_1 , and C_2 related to the focalization efficiency are calculated via integration of the incident electric field vector components over the effective irradiated volume. All of these parameters are dependent on the angular semi-aperture of the objective ($\theta_m = 64.16^\circ$ for the $100\times$ lens with a numerical aperture equal to 0.9) and on the

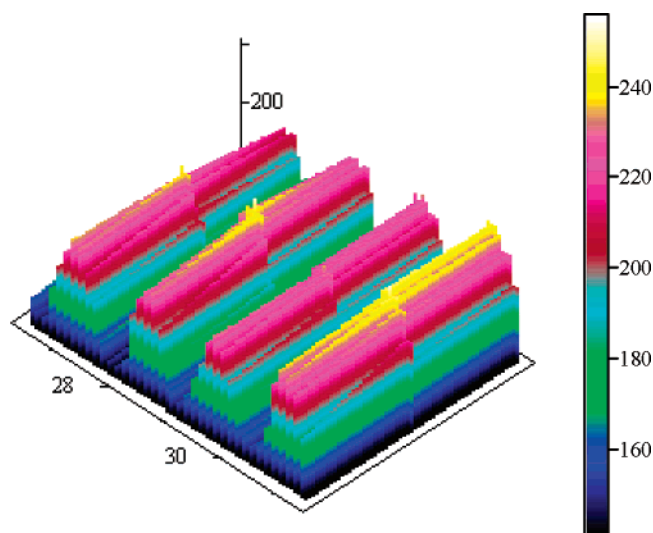


Figure 7. Enlarged view in three dimensions of the Raman image obtained over a $5 \times 10 \mu\text{m}^2$ area of the first grating in the (YY) polarization conditions (see Figure 5b) showing the high spatial experimental resolution at near the diffraction limit ($\lambda/2$).

refractive index of the sample ($n \approx 1.50$); here, the A and B parameter values are equal to 3.579 and 0.737, respectively, and the coefficients C_0 , C_1 , and C_2 were numerically computed and found equal to 6.2273, 0.1988, and 0.0042, respectively (results of unpublished work).

Survey Raman Spectra. Some Raman spectra were first recorded using an isotropic sample in order to find out the best conditions for further polarization studies. Using the 752.5 nm red line excitation, satisfactory fluorescence free Raman results were obtained for a polymer film since, according to UV–visible absorption data, the homopolymer displays only a very intense band at near 470 nm assigned to $\pi \rightarrow \pi^*$ type transitions.^{49,50} Similarly, polarized Raman spectra with a good signal-to-noise ratio were obtained using the first holographic grating sample. As shown in Figure 4, the spectra recorded in the $700\text{--}1700 \text{ cm}^{-1}$ wavenumber range exhibit intense bands at 1107 cm^{-1} ($\nu_{\text{C-N}}$, 18a), 1137 and 1200 cm^{-1} (δCH ring, 9a, 9b), 1339 cm^{-1} ($\nu_{\text{s NO}_2}$), 1394 cm^{-1} ($\nu_{\text{N=N}}$), 1425 and 1447 cm^{-1} (δCH ring, 19a, 19b), 1572 and 1592 cm^{-1} ($\omega\text{C=C}$, 8a, 8b) characteristic of the “trans” azobenzene chromophore.^{56,60,61} In addition, the two YY and YX polarized spectra display strong intensity variations confirming the existence of dye orientational effects. In the following, to establish the variations of the polarized Raman intensities in various regions of a grating, we have selected the whole $1045\text{--}1180 \text{ cm}^{-1}$ spectral domain, as indicated by the vertical arrows on Figure 4.

Polarization Analyses and Corresponding Raman Images for the First Grating ($\eta = 1.5\%$). Two series of typical polarized Raman spectra were recorded in the whole $200\text{--}1800 \text{ cm}^{-1}$ range on a surface area of about $5 \times 10 \mu\text{m}^2$ for both $Z(\text{YY})\bar{Z}$ and $Z(\text{YX})\bar{Z}$ scattering geometries in the first experimental configuration (Figure 1a) and, similarly, for both $Z(\text{XX})\bar{Z}$ and $Z(\text{XY})\bar{Z}$ geometries in the second configuration (Figure 1b). After intensity integrations over the $1045\text{--}1180 \text{ cm}^{-1}$ range, two-dimensional plots of the Raman intensity variations are built, and they lead to the couples of polarized Raman images reported on Figures 5 and 6, respectively. These images nicely reproduce the $\approx 1.37 \mu\text{m}$ period spacing, and as expected, they correspond to intensity profiles along the $X(\delta)$ direction which are not exactly in-phase but exhibit a rather weak dephasing in both couples of spectra. We thus conclude that the main

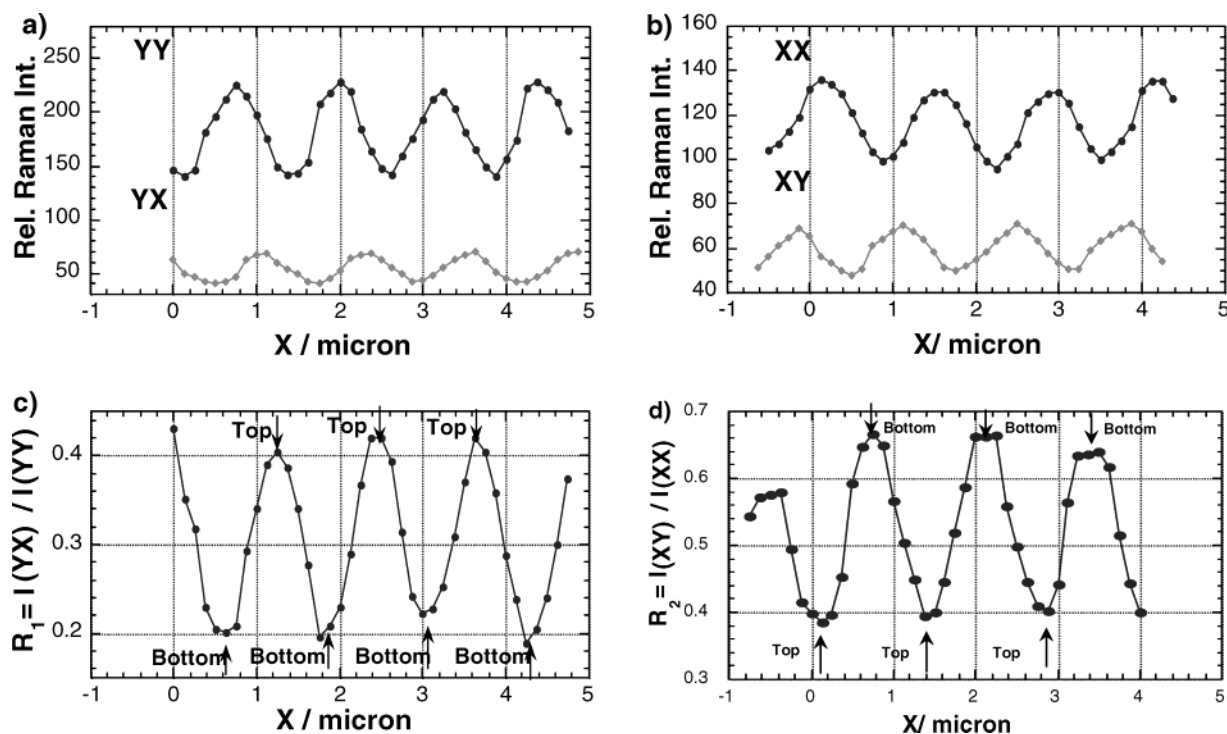











Figure 8. Variations of the polarized Raman integrated intensities on the surface of the first grating along the \bar{X} vector grating direction under (a) the (YY) and (YX) polarizations and (b) the (XX) and (XY) scattering geometries; corresponding variations of the intensity ratios (c) $R_1(\delta)$ and (d) $R_2(\delta)$, whose values are used in the calculation of the order parameters.

TABLE 1: Final Values of the Order Parameters, $\langle P_2 \rangle$ and $\langle P_4 \rangle$, and the Lagrange's Multipliers, λ_2 and λ_4 , According to the "Information Entropy Theory" in Various Regions of the Surface Relief of the Three Investigated Gratings

Position	+45°, +135° Configuration						Initial incident field	Type of distribution function
	R ₁	R ₂	$\langle P_2 \rangle$	$\langle P_4 \rangle$	λ_2	λ_4		
a) $\eta=1.5\%$								
0.0 (Tops)	0.419	0.395	-0.013	-0.012	-0.066	-0.109		Nearly Isotropic
$\Lambda/4, 3\Lambda/4$	0.310	0.525	+0.008	+0.008	+0.041	+0.074		Nearly Isotropic
$\Lambda/2$ (Bottoms)	0.202	0.655	-0.277	+0.132	-1.567	+1.081		Strong maximum at 90°
b) $\eta=2.7\%$								
0.0 (Tops)	0.604	0.521	-0.005	-0.174	-0.359	-2.048		Bimodal asym. $\pm 51^\circ$
$\Lambda/4, 3\Lambda/4$	0.534	0.562	+0.028	-0.168	-0.015	-1.824		Bimodal asym. $\pm 49^\circ$
$\Lambda/2$ (Bottoms)	0.464	0.604	-0.037	-0.136	-0.498	-1.598		Bimodal asym. $\pm 52^\circ$
c) $\eta=1.2\%$								
0.0 (Tops)	0.575	0.552	+0.021	-0.182	-0.132	-2.065		Bimodal asym. $\pm 50^\circ$
$\Lambda/4, 3\Lambda/4$	0.477	0.686	+0.033	-0.183	+0.010	-2.031		Bimodal asym. $\pm 49^\circ$
$\Lambda/2$ (Bottoms)	0.380	0.820	-0.140	-0.113	-1.827	-2.167		Bimodal asym. $\pm 58^\circ$

orientational effects on the dye molecules are correctly predicted using the AHB model. More importantly, as shown in Figure 7, a three-dimensional plot of the $Z(YY)\bar{Z}$ polarized Raman image containing four grating periods ($\Lambda = 1.37 \mu\text{m}$) exhibits nice intensity contrasts between the wide valleys and strong peaks, so that the intensity variations in the slope regions are well resolved: this demonstrates that we are actually working at the diffraction limit since a quarter of period ($\approx 0.350 \mu\text{m}$) is roughly equal to the half wavelength, $\lambda/2$ ($\approx 0.376 \mu\text{m}$).

Furthermore, it is noteworthy that the related video white lamp transmission images, which are reported above the Raman images in order to better figure out the laser scanned grating area, display also contrasted groove lines. However, depending on the focus conditions, the observed darken lines were corresponding either to ridges (Figure 5) or to tops (Figure 6) of the grating grooves; one may thus arrive to misleading interpretations when using these video images. So, the following treatments were more confidently performed by scaling the data

with respect to the intensity maxima in the $Z(Y\bar{Y})\bar{Z}$ and $Z(X\bar{X})\bar{Z}$ spectra, respectively.

The Raman intensities observed at each $\pm 0.125 \mu\text{m}$ sample displacement along the grating vector direction are now carefully analyzed in the two series of experiments. The intensity variations along a four period distance were first averaged over the three scanned lines, and they gave rise to results reported in Figure 8, along with the variations of the related $R_1(\delta)$ and $R_2(\delta)$ intensity ratios. Even though there are some dispersed and scattered points, the above experimental results allow us to detect significant variations in the $R_1(\delta)$ and $R_2(\delta)$ ratios and, as expected, these values are maximizing at the top and bottom regions of the surface relief, respectively. Actually, the $R_1(\delta)$ and $R_2(\delta)$ ratios are varying over the 0.42–0.20 and 0.40–0.66 ranges, respectively: this indicates that the orientational order parameters $\langle P_2 \rangle$ and $\langle P_4 \rangle$ are also varying along a grating period.

Under these conditions, we have considered a more probable couple of $R_1(\delta)$ and $R_2(\delta)$ values at each surface position, with a particular attention not only at top ($X = 0$) and bottom ($X = \Lambda/2$) locations but also at the half-slope points (i.e. at $X = \Lambda/4$ and $3\Lambda/4$, respectively). All of the calculations are then performed by using the theoretical general intensity expressions (see eqs 10–13) and the corresponding estimates of the $\langle P_2 \rangle$ and $\langle P_4 \rangle$ coefficients along with the type of the calculated distribution functions are reported in Table 1.

First, it must be pointed out that, at the $X = \Lambda/4$ and $3\Lambda/4$ positions, where the incident electric field was circularly polarized, calculated values for the $\langle P_2 \rangle$ and $\langle P_4 \rangle$ order parameters are very weak and nearly equal to zero, $+0.008$ in both cases. We thus conclude that in these regions the photoinduced effects have not markedly perturbed the in-plane chromophore orientations, and their distribution functions remain nearly isotropic. These convincing results confirm that the developed theoretical approach and the applied method are physically consistent.

Now, in the other grating regions, it is remarkable that the $\langle P_2 \rangle$ parameter is always negative, but its absolute value is relatively weak at $X = 0$ (-0.013) and quite large at $X = \Lambda/2$ (-0.277). This demonstrates that the principal long axis of the azobenzene molecules is always reorientated perpendicularly to the electric field vector of the actinic light, and the orientational effects are surely more pronounced in the bottom regions. Nevertheless, the related $\langle P_2 \rangle$ value is very far from the -0.5 limit expected for a complete ordering of all of the chromophores and the orientations are probably spread over a wide range. In fact, more information about the shape and width of the molecular distribution functions are precisely delivered by looking at the $\langle P_4 \rangle$ parameter which takes a negative value at $X = 0$ (-0.012) and a positive one at $X = \Lambda/2$ ($+0.132$).

From the two first even parity order parameters, we are now able to estimate the most probable orientational distribution functions, $f(\theta)$, following the “Information Entropy” theory.^{48,62–64} In this approach, the distribution function is obtained by maximizing the information entropy and the Lagrange’s method of undetermined multipliers leads to the function

$$f(\theta) = Z^{-1} \exp[\lambda_2 P_2(\cos \theta) + \lambda_4 P_4(\cos \theta)] \quad (14)$$

where λ_2 and λ_4 are the Lagrange’s multipliers and Z denotes a normalization constant

$$Z = \int_{-1}^{+1} d(\cos \theta) \exp[\lambda_2 P_2(\cos \theta) + \lambda_4 P_4(\cos \theta)] \quad (15)$$

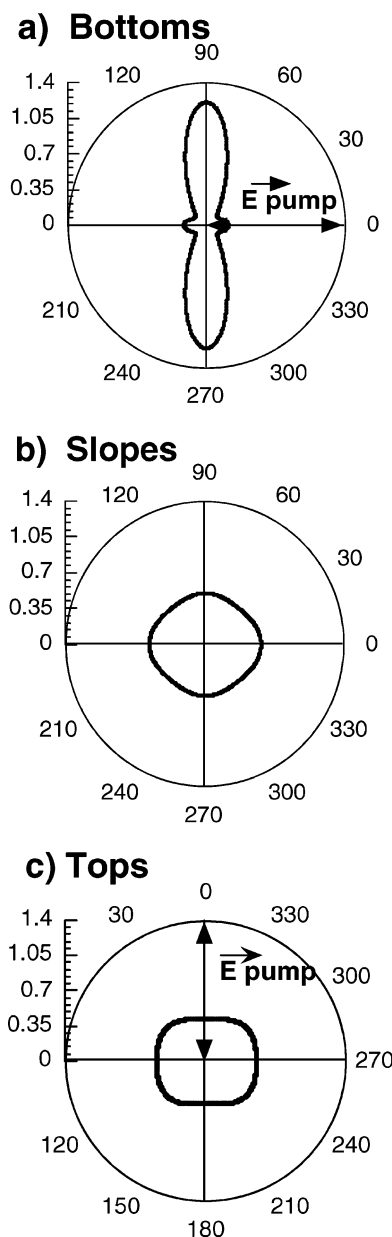


Figure 9. Polar representations of the chromophore distribution functions in the first grating at (a) the bottom, (b) the slope and, (c) the top regions of the surface relief.

Therefore, λ_2 and λ_4 were numerically calculated, and their values in the bottom, slope, and top regions are reported in Table 1. The corresponding normalized functions $f(\theta)$ are then estimated, and their plots in a polar coordinate system are shown in Figure 9. These distributions are drastically different: in the bottom regions, a major fraction of probed molecules is actually oriented perpendicularly to the actinic light, since the more intense maxima are observed at 90° and 270° (Figure 9a); in contrast, in the slope regions, the distributions are nearly isotropic, as expected (Figure 9b), and in the peak regions, some orientation effects are not yet clearly evidenced (Figure 9c). So, we arrive to the conclusion that after the first writing procedure the chromophore orientation distributions are anisotropic only in the bottom positions, where the incident beam intensity was maximum and the isomerization process was dominant; a large surface relief modulation has already developed but both the phase and amplitude gratings have not yet been interfering constructively in all regions.

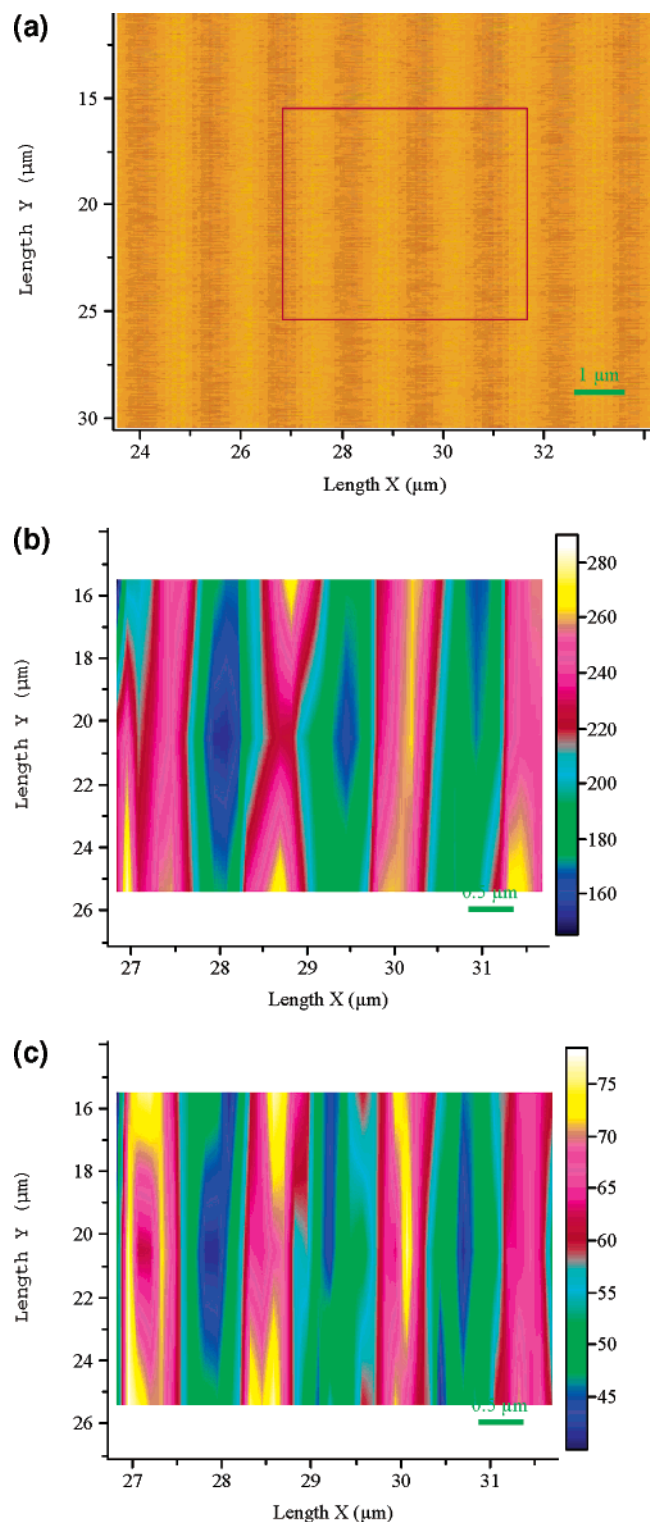


Figure 10. Video image (a) and Raman images obtained over a $5 \times 10 \mu\text{m}^2$ area of the second grating ($\eta = 2.7\%$) under (b) the (YY) and (c) the (YX) polarization conditions, using the first experimental configuration described in Figure 1a.

Polarization Analyses and Corresponding Raman Images for the Second Grating ($\eta = 2.7\%$). Similarly, various polarized Raman spectra were recorded using the second grating inscribed under the same conditions and, then, irradiated with a “RCP” beam during a short period of 50 s; this grating was displaying a diffraction efficiency increase up to a plateau value of 2.7%. In both experimental configurations, i.e., the recording of the $Z(YY)\bar{Z}$ and $Z(YX)\bar{Z}$ spectra on one hand (Figure 10)

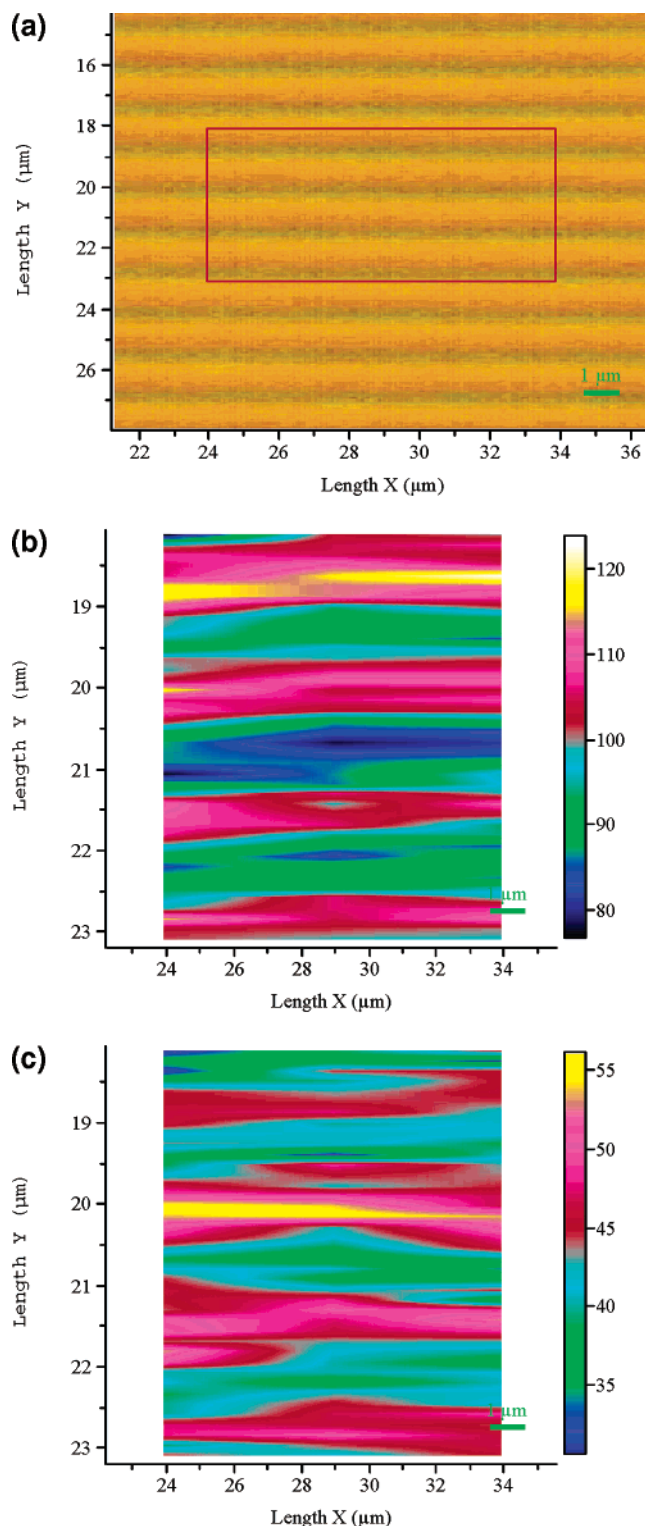


Figure 11. Video image (a) and Raman images obtained over a $5 \times 10 \mu\text{m}^2$ area of the second grating ($\eta = 2.7\%$) under (b) the (XX) and (c) the (XY) polarization conditions, using the second experimental configuration described in Figure 1b.

and the $Z(XX)\bar{Z}$ and $Z(XY)\bar{Z}$ spectra on the other hand (Figure 11), the intensity integrations lead again to nicely resolved polarized Raman images from a surface area of about $5 \times 10 \mu\text{m}^2$. Similar data treatments were thus carried out to obtain the different intensity variations and intensity ratios as reported in Figure 12. It is noteworthy that the $R_1(\delta)$ and $R_2(\delta)$ ratios are now varying over more restricted domains, namely in the 0.61–0.46 and 0.52–0.61 ranges, respectively; this probably

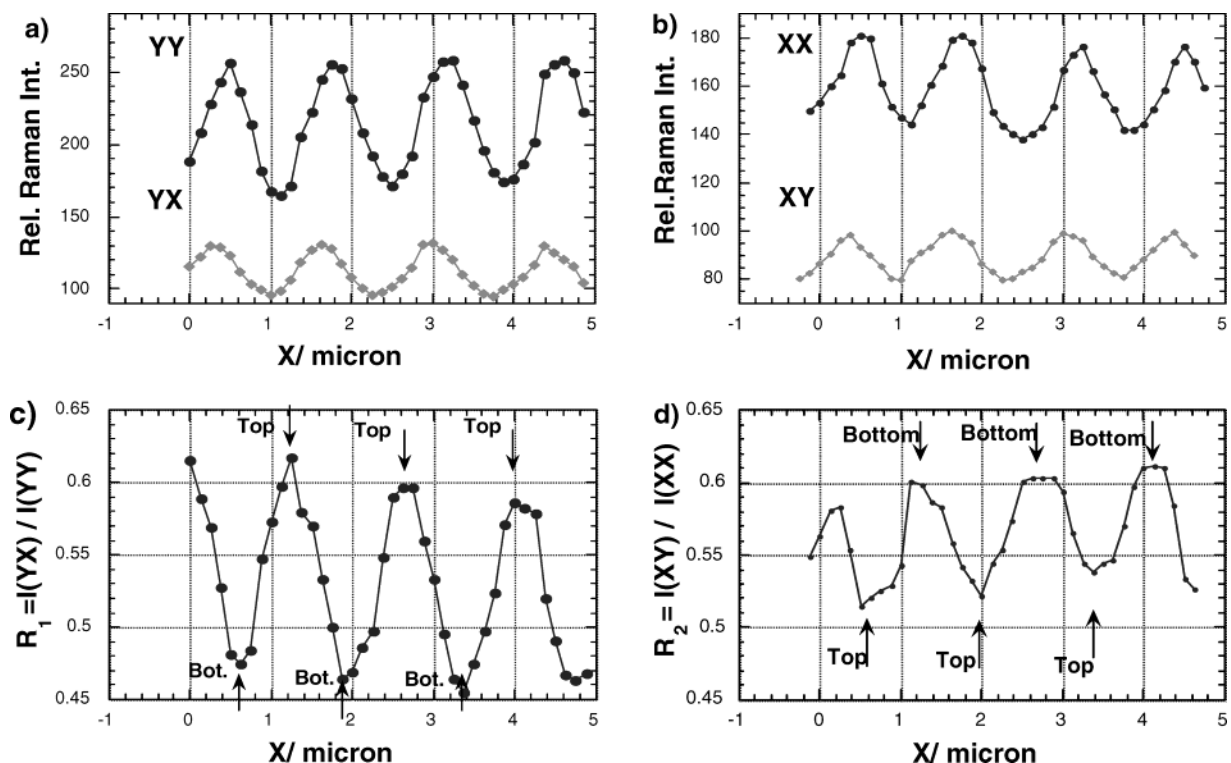


Figure 12. Variations of the polarized Raman integrated intensities on the surface of the second grating ($\eta = 2.7\%$) along the \vec{X} vector grating direction under (a) the (YY) and (YX) polarizations and (b) the (XX) and (XY) scattering geometries; corresponding variations of the intensity ratios (c) $R_1(\delta)$ and (d) $R_2(\delta)$, whose values are used in the calculation of the order parameters.

indicates that the orientational order parameters $\langle P_2 \rangle$ and $\langle P_4 \rangle$ are not varying to a large extent along a grating period; however, the $R_1(\delta)$ values are still maximizing at the top regions, whereas the $R_2(\delta)$ ones show maxima in the bottom regions. Under these conditions and as shown in Table 1, the $\langle P_2 \rangle$ and $\langle P_4 \rangle$ coefficients are estimated and the Lagrange' multipliers λ_2 and λ_4 are numerically calculated in order to construct the corresponding distribution functions (Figure 13).

First, it must be pointed out that at the $X = \Lambda/4$ and $3\Lambda/4$ positions, where the initial incident electric field for grating inscription was circularly polarized, the calculated values for the $\langle P_2 \rangle$ and $\langle P_4 \rangle$ order parameters differ now from zero, and they are equal to $+0.028$ and -0.168 , respectively. Surprisingly, the "RCP" single beam has markedly perturbed in these regions the previously isotropic orientations and the chromophore distribution function appears bimodal asymmetric with maxima at near $\pm 49^\circ$ (Figure 13b).

Then, in the other grating regions, it is remarkable that the $\langle P_2 \rangle$ parameter is always very weak, -0.005 at $X = 0$ and -0.037 at $X = \Lambda/2$, whereas the $\langle P_4 \rangle$ values are negative and quite large, -0.174 and -0.136 , respectively. This demonstrates that the forms of distribution functions are now dominated by the $\langle P_4 \rangle$ coefficient and, actually, they become bimodal asymmetric in shape, with maxima at near $\pm 51^\circ$ (Figure 13, parts a and c).

We definitively conclude that, after a short time "RCP" irradiation, the observed increases in stability and in efficiency of this grating stem from the existence of a new birefringence contribution in all parts of the invariant sinusoidal relief structure; this new contribution is superimposed to the initial birefringence, which was probably poorly efficient and markedly erased by the growing surface relief grating. From this micro-Raman study carried out using various polarization conditions and in contrast with previous assumptions,^{34,39} we can no longer argue that the efficiency increases (often observed after a short

irradiation and upon relaxation) are due to mechanical and thermal constraints and/or to cis-trans back isomerizations but, preferentially, to significant orientational molecular ordering effects.

Polarization Analyses and Corresponding Raman Images for the Partly Erased Grating ($\eta = 1.2\%$). A quite similar polarized Raman study has been accomplished on the grating erased during a longer period of ≈ 800 s; its diffraction efficiency has significantly decreased down to 1.2% (Figure 2) as well as its surface relief modulation which is now equal to ≈ 66 nm (Figure 3). However, it is important to note that, as compared to the first inscribed grating ($\eta = 1.5\%$, $\Delta h = 114$ nm), these values represent a substantial fraction of the initial efficiency ($\approx 80\%$) and of the relief modulation ($\approx 58\%$), respectively. This demonstrates again that the $(+45^\circ, +135^\circ)$ optical configuration for grating inscription in conjunction with a "RCP" irradiation may be very efficient for duplication and phase mask applications.³⁹

In fact, from the intensity integrations on the two couples of polarized Raman spectra, $Z(YY)\bar{Z} - Z(YX)\bar{Z}$ on one hand and $Z(XX)\bar{Z} - Z(XY)\bar{Z}$ on the other hand, we have again obtained nicely resolved Raman images (not shown here) and $R_1(\delta)$ and $R_2(\delta)$ ratios varying over similar restricted domains, namely in the $0.58-0.38$ and $0.55-0.82$ ranges, respectively (Table 1); this indicates that the orientational order parameters $\langle P_2 \rangle$ and $\langle P_4 \rangle$ have not been significantly changed during the erasure process and that the distribution functions are still mainly governed by the $\langle P_4 \rangle$ values. Indeed, after calculation of the Lagrange' multipliers, λ_2 and λ_4 , the corresponding distribution functions are again found bimodal, asymmetric in shape and with maxima at $\pm 58^\circ$, $\pm 49^\circ$, and $\pm 50^\circ$ in the bottom, slope, and peak regions, respectively (Table 1).

We thus conclude that, after a longer time (≈ 800 s) of "RCP" irradiation, the observed decreases in efficiency stem from a partly erasure of the surface relief, whereas the birefringence

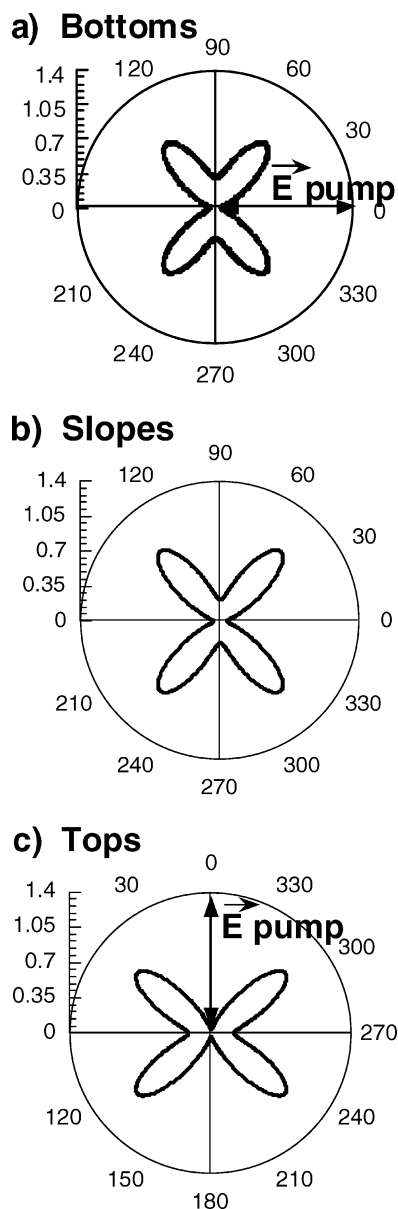


Figure 13. Polar representations of the chromophore distribution functions in the second grating ($\eta = 2.7\%$) at (a) the bottom, (b) the slope and, (c) the top regions of the surface relief.

contributions in all regions are probably perturbed to a less extent, as inferred from the observed similar chromophore orientation distribution functions. From this micro-Raman study coupled with AFM results, we conclude that in such gratings, once formed, it is easier to erase the surface relief than to perturb the molecular orientations by using a single “RCP” beam; a similar situation does not probably apply when using a linearly “p” polarized beam since the erasure kinetics were found always more rapid and efficient in that case and the major part of the surface relief was rapidly disappearing.³⁹

V. Conclusions

In this study, we have investigated the molecular orientation processes involved during the writing of a holographic grating on a p(DR1M) homopolymer film using two orthogonal and linearly polarized (+45°, +135°) laser beams and during the first steps of the grating post-irradiation using a single beam of circular “RCP” polarization. In our spectroscopic approach, we have performed various confocal polarized micro-Raman ex-

periments in order to get the opportunity to precise the orientational distribution functions of the chromophores in all regions, well, slope, and peak, of the surface relief gratings. Also, we have combined these results with AFM topographic data and afforded new information at the molecular level about the relative contributions of the birefringence and surface modulation gratings. We thus conclude that, after a short time “RCP” irradiation of a low diffraction efficiency grating, the increase in diffraction is not due to any change in the amplitude of the surface modulation but to a marked increase in birefringence contributions. Then, after a longer time “RCP” irradiation, a substantial fraction of the initial diffraction efficiency (80%) and a strong anisotropy in the chromophore orientations are maintained, whereas the surface relief modulation is partly erased (58%).

Finally, it is noteworthy that all of the polarization configurations used in this study appear efficient for grating inscription as well as for grating duplication and this could open new routes in phase mask applications. Such works in that direction are in progress, and they will be published in due course.

Acknowledgment. The authors are indebted to the CNRS (Chemistry Department) and to Région Aquitaine for financial support in AFM and micro-Raman equipments. They are thankful to A. Natansohn, Queen’s University, Ontario (Canada), for providing the functionalized homopolymer sample.

References and Notes

- (1) Rochon, P.; Mao, J.; Natansohn, A.; Batalla, E. *Polym. Prepr.* **1994**, *35*, 154.
- (2) Rochon, P.; Batalla, E.; Natansohn, A. *Appl. Phys. Lett.* **1995**, *66*, 136.
- (3) Barrett, C. J.; Natansohn, A. L.; Rochon, P. L. *J. Phys. Chem. B* **1996**, *100*, 8836.
- (4) Kim, D. Y.; Tripathy, S. K.; Li, L.; Kumar, J. *Appl. Phys. Lett.* **1995**, *66*, 1166.
- (5) Kim, D. Y.; Li, L.; Jiang, X. L.; Shivshankar, V.; Kumar, J.; Tripathy, S. K. *Macromolecules* **1995**, *28*, 8835.
- (6) Jiang, X. L.; Li, L.; Kumar, J.; Kim, D. Y.; Shivshankar, V.; Tripathy, S. K. *Appl. Phys. Lett.* **1996**, *68*, 2618.
- (7) Barrett, C. J.; Rochon, P. L.; Natansohn, A. L. *J. Chem. Phys.* **1998**, *109*, 1505.
- (8) Chen, J. P.; Lagugné-Labarthe, F.; Natansohn, A.; Rochon, P. *Macromolecules* **1999**, *32*, 8572.
- (9) Yager, K. G.; Barrett, C. J. *Curr. Opin. Solid State Mater. Sci.* **2001**, *5*, 487.
- (10) Natansohn, A.; Rochon, P. *Chem. Rev.* **2002**, *102*, 4139–4176.
- (11) Bian, S.; Liu, W.; Williams, J. M.; Samuelson, L.; Kumar, J.; Tripathy, S. K. *Chem. Mater.* **2000**, *12*, 1585.
- (12) Tripathy, S. K.; Viswanathan, N. K.; Balasubramanian, S.; Kumar, J. *Polym. Adv. Technol.* **2000**, *11*, 570.
- (13) Naydenova, I.; Nikolova, L.; Todorov, T.; Holme, N. C. R.; Ramanujam, P. S.; Hvilsted, S. *J. Opt. Soc. Am. B* **1998**, *15*, 1257.
- (14) Pedersen, M.; Johansen, P. M.; Holme, N. C. R.; Ramanujam, P. S.; Hvilsted, S. *Phys. Rev. Lett.* **1998**, *80*, 89.
- (15) Lagugné Labarthe, F.; Buffeteau, T.; Sourisseau, C. *J. Phys. Chem. B* **1998**, *102*, 2654.
- (16) Lagugné Labarthe, F.; Buffeteau, T.; Sourisseau, C. *J. Phys. Chem. B* **1998**, *102*, 5754.
- (17) Lagugné Labarthe, F.; Buffeteau, T.; Sourisseau, C. *J. Phys. Chem. B* **1999**, *103*, 6690.
- (18) Lagugné Labarthe, F.; Rochon, P.; Natansohn, A. *Appl. Phys. Lett.* **1999**, *75*, 1377.
- (19) Lagugné Labarthe, F.; Bruneel, J. L.; Buffeteau, T.; Sourisseau, C.; Huber, M. R.; Zilker, S. J.; Bieringer, T. *Phys. Chem. Chem. Phys.* **2000**, *2*, 5154.
- (20) Lagugné Labarthe, F.; Bruneel, J. L.; Sourisseau, C.; Huber, M. R.; Börgen, V.; Menzel, H. *J. Raman Spectrosc.* **2001**, *32*, 665.
- (21) Lagugné Labarthe, F.; Buffeteau, T.; Sourisseau, C. *Appl. Phys. B* **2002**, *74*, 129.
- (22) Lagugné Labarthe, F.; Buffeteau, T.; Sourisseau, C. *J. Appl. Phys.* **2001**, *90*, 3149.
- (23) Fiorini, C.; Prudhomme, N.; de Veyrac, G.; Maurin, I.; Raimond, P.; Nunzi, J. M. *Synth. Met.* **2000**, *115*, 121.

- (24) Chaput, F.; Bateau, J.; Lahlil, K.; Boilot, J. P.; Darracq, B.; Levy, Y.; Peretti, J.; Safarov, V. I.; Parent, G.; Fernandez-Acebes, A.; Lehn, J.-M. *Mol. Cryst. Liq. Cryst.* **2000**, *344*, 77.
- (25) Frey, L.; Darracq, B.; Chaput, F.; Lahlil, K.; Jonathan, J.-M.; Roosen, G.; Boilot, J. P.; Levy, Y. *Opt. Comm.* **2000**, *173*, 11.
- (26) Bublit, D.; Fleck, B.; Wenke, L. *Appl. Phys. B* **2001**, *72*, 931.
- (27) Cipparrone, G.; Mazulla, A.; Russo, G. *Appl. Phys. Lett.* **2001**, *78*, 1186.
- (28) Sumaru, K.; Yamanaka, T.; Fukuda, T.; Matsuda, H. *Appl. Phys. Lett.* **1999**, *75*, 1878.
- (29) Wu, Y.; Natansohn, A.; Rochon, P. *Macromolecules* **2001**, *34*, 7822.
- (30) Zilker, S. J.; Huber, M. R.; Bieringer, T.; Haarer, D. *Appl. Phys. B* **1999**, *68*, 893.
- (31) Cimrova, V.; Neher, D.; Kostromine, S. G.; Bieringer, T. *Macromolecules* **1999**, *32*, 8496.
- (32) Cimrova, V.; Neher, D.; Hildebrandt, R.; Hegelich, M.; von der Lieth, A.; Marowsky, G.; Hagen, R.; Kostromine, S. G.; Bieringer, T. *Appl. Phys. Lett.* **2002**, *81*, 1228.
- (33) Zhang, Y.; Lu, Z.; Deng, X.; Liu, Y.; Zhao, Y. *Opt. Comm.* **2003**, *220*, 289.
- (34) Jiang, X. L.; Li, L.; Kumar, J.; Kim, D. Y.; Tripathy, S. K. *Appl. Phys. Lett.* **1998**, *72*, 2502.
- (35) Li, L.; Jiang, X. L.; Kim, D. Y.; Kumar, J.; Tripathy, S. K. Proceedings of "Organic thin films for photonics applications"; ACS (POLY/PMSE) and OSA, Technical Digest Series: OSA: Washington, DC, 1997; Vol. 14, p 214.
- (36) Yamamoto, T.; Hasegawa, M.; Kanazawa, A.; Shiono, T.; Ikeda, T. *J. Mater. Chem.* **2000**, *10*, 337.
- (37) Yamamoto, T.; Yoneyama, S.; Tsutsumi, O.; Kanazawa, A.; Shiono, T.; Ikeda, T. *J. Appl. Phys.* **2000**, *88*, 2215.
- (38) Bieringer, T.; Wuttke, R.; Haarer, D.; Gebner, U.; Rübner, J. *Macromol. Chem. Phys.* **1995**, *196*, 1375.
- (39) Lagugné Labarthe, F.; Buffeteau, T.; Sourisseau, C. *Phys. Chem. Chem. Phys.* **2002**, *4*, 4020.
- (40) Hill, K. O.; Malo, B.; Bilodeau, F.; Johnson, D. C.; Albert, J. *Appl. Phys. Lett.* **1993**, *62*, 1035.
- (41) Malo, B.; Johnson, D. C.; Bilodeau, F.; Albert, J.; Hill, K. O. *Opt. Lett.* **1993**, *18*, 1277.
- (42) Tsunetomo, K.; Koyama, T. *Opt. Lett.* **1997**, *22*, 411.
- (43) Xia, Y.; Rogers, J. A.; Paul, K. E.; Whitesides, G. M. *Chem. Rev.* **1999**, *99*, 1823.
- (44) Wu, M. H.; Whitesides, G. M. *Adv. Mat.* **2002**, *14*, 1502.
- (45) Peng, J.; Han, Y.; Yang, Y.; Li, B. *Polymer* **2003**, *44*, 2379.
- (46) Coufal, H. J.; Pasaltis, D.; Sincerbos, G. *Holographic Data Storage*; Springer-Verlag: New York, 2000.
- (47) Lagugné Labarthe, F.; Buffeteau, T.; Sourisseau, C. *Macromol. Symp.* **1999**, *137*, 75.
- (48) Lagugné Labarthe, F.; Buffeteau, T.; Sourisseau, C. *Appl. Spectrosc.* **2000**, *54*, 699.
- (49) Natansohn, A.; Rochon, P.; Gosselin, J.; Xie, S. *Macromolecules* **1992**, *25*, 2268.
- (50) Brown, D.; Natansohn, A.; Rochon, P. *Macromolecules* **1995**, *28*, 6116.
- (51) Helgert, M.; Fleck, B.; Wenke, L.; Hvilsted, S.; Ramanujam, P. *S. Appl. Phys. B* **2000**, *70*, 803.
- (52) Sekkat, Z.; Dumont, M. *Synth. Met.* **1993**, *54*, 373.
- (53) Dumont, M. *Photoact. Org. Mol., Sci. Appl.* **1996**, *9*, 501.
- (54) Dumont, M.; El Osman, A. *Chem. Phys.* **1999**, *245*, 437.
- (55) Lagugné Labarthe, F.; Sourisseau, C. *New J. Chem.* **1997**, *21*, 879.
- (56) Lagugné Labarthe, F.; Sourisseau, C. *J. Raman Spectrosc.* **1996**, *27*, 491.
- (57) Turrell, G. *J. Raman Spectrosc.* **1984**, *15*, 103.
- (58) Brémard, C.; Laureyns, J.; Turrell, G. *Can. J. Spectrosc.* **1987**, *32*, 70.
- (59) Turrell, G. In *Practical Raman Spectroscopies*; Gardiner, D. J., Graves, P. R., Eds.; Springer-Verlag: Berlin, 1989; Chapter 2, p 13.
- (60) Biswas, N.; Umapathy, S. *J. Phys. Chem. A* **2000**, *104*, 2734.
- (61) Biswas, N.; Umapathy, S. *J. Raman Spectrosc.* **2001**, *32*, 471.
- (62) Berne, B. J.; Pechukas, P.; Harp, G. D. *J. Chem. Phys.* **1968**, *49*, 3125.
- (63) Kinoshita, K. J.; Kawato, S.; Ikegami, A. *Biophys. J.* **1977**, *20*, 289.
- (64) Pottel, H.; Herreman, W.; Van der Meer, B. W.; Ameloot, M. *Chem. Phys.* **1986**, *102*, 37.